MOX-Report No. 11/2026

Optimized Schwarz Waveform Relaxation for the Damped Wave Equation

Cicalese, G.; Ciaramella, G.; Mazzieri, I.; Gander, M. J.

Optimized Schwarz Waveform Relaxation for the Damped Wave Equation

Gerardo Cicalese[0000-0001-5061-8608] and
Gabriele Ciaramella[0000-0002-5877-4426] and
Ilario Mazzieri[0000-0003-4121-8092] and
Martin J. Gander[0000-0001-8450-9223]

1 Introduction

The development of transmission conditions in overlapping Schwarz Waveform Relaxation (SWR) methods for the undamped wave equation has progressed from classical Dirichlet to absorbing conditions. While Dirichlet conditions produce strong interface reflections that slow down convergence, absorbing conditions reduce error reflections and promote efficient wave transmission between subdomains [1–3].

In this paper, we investigate general transmission conditions for the (one-dimensional) damped wave equation, for which no practical transparent conditions are available in the literature. In particular, for a domain $\Omega = (0, L)$ and time $t \geq 0$, we consider the viscoelastic-telegrapher damped wave equation

$$\partial_{tt}u + \gamma\partial_t u = c^2\partial_{xx}u + \nu\partial_t\partial_{xx}u + f, \quad \text{in } \Omega, \tag{1}$$

with initial conditions $u(x, 0) = u_0(x),\ \partial_t u(x, 0) = v_0(x),\ x \in \Omega$, and homogeneous Dirichlet boundary conditions $u(0, t) = u(L, t) = 0,\ t > 0$. Here, γ represents the telegrapher damping and ν the viscoelastic damping. Problem (1) is hyperbolic when $\nu = 0$ [7] and not hyperbolic when $\nu > 0$ [6].

For this model, we investigate transmission conditions characterized by two parameters that can be tuned to optimize SWR convergence. We consider a spectral optimization framework that automatically identifies the optimal parameters. This relies on a frequency-domain analysis to derive a closed-form expression for the SWR convergence factor, which we then minimize (numerically) using two different metrics. The proposed approach provides a systematic way to tune the transmis-

---

Gerardo Cicalese, Gabriele Ciaramella, Ilario Mazzieri
MOX Laboratory, Dipartimento di Matematica, Politecnico di Milano, Piazza Leonardo da Vinci 32, 20133 Milano, Italia, e-mail: gerardo.cicalese, gabriele.ciaramella, ilario.mazzieri@polimi.it

Martin J. Gander
Section de mathématiques, Université de Genève, Rue du Conseil-Général 9, CP 64, 1211 Genève 4, Suisse, e-mail: martin.gander@unige.ch

sion conditions. It turns out that our approach significantly accelerates the SWR convergence in the case of viscoelastic damping.

To define the SWR method for our model problem (1), we decompose $\Omega = (0, L)$ into two overlapping subdomains $\Omega_1 = (0, b)$ and $\Omega_2 = (a, L)$ with $0 < a < b < L$ and overlap $\delta = b - a > 0$. The SWR iterations are then defined as

$$\partial_{tt} v^{(k+1)} + \gamma \partial_t v^{(k+1)} = c^2 \partial_{xx} v^{(k+1)} + \nu \partial_t \partial_{xx} v^{(k+1)} + f, \qquad \text{in } \Omega_1, \tag{2}$$

$$\big(\partial_x + \Lambda\big) v^{(k+1)}(b, t) = \big(\partial_x + \Lambda\big) w^{(k)}(b, t), \tag{3}$$

$$\partial_{tt} w^{(k+1)} + \gamma \partial_t w = c^2 \partial_{xx} w^{(k+1)} + \nu \partial_t \partial_{xx} w^{(k+1)} + f, \qquad \text{in } \Omega_2, \tag{4}$$

$$\big(\partial_x - \Lambda\big) w^{(k+1)}(a, t) = \big(\partial_x - \Lambda\big) v^{(k)}(a, t), \tag{5}$$

where k is the iteration index and $\Lambda = p\partial_t + q$ with $p, q \in \mathbb{R}$. Notice that the classical transparent condition for $\gamma = \nu = 0$ corresponds to $(p, q) = (1/c, 0)$ [1, 3].

The paper is organized as follows. In Section 2, we derive the convergence factor and introduce two optimization strategies. In Section 3, we present numerical experiments, including convergence analyses for telegrapher and viscoelastic damping with various parameters, and we examine how optimized transmission-condition parameters vary with the damping coefficients. We present our conclusions in Section 4.

2 Convergence Factor and Optimization Strategies

For the error analysis, we set $f \equiv 0$, use the Laplace transform in time, and denote by $\widehat{u}(x, s)$ the Laplace-transformed field. From (1) we get

$$\partial_{xx} \widehat{u} = -\kappa^2(s) \widehat{u}, \tag{6}$$

where $\kappa(s) := -\mathrm{i}\, s/c \sqrt{\left(1 + \gamma s^{-1}\right) / \left(1 + \nu c^{-2} s\right)}$ and i is the imaginary unit. To derive the convergence factor, we first solve (6) in each subdomain and apply the homogeneous Dirichlet boundary conditions to get

$$\widehat{v}(x, s) = A_v(s) \left(e^{\mathrm{i}\kappa(s)x} - e^{-\mathrm{i}\kappa(s)x} \right), \tag{7}$$

$$\widehat{w}(x, s) = A_w(s) \left(e^{\mathrm{i}\kappa(s)x} - e^{2\mathrm{i}\kappa L} e^{-\mathrm{i}\kappa(s)x} \right). \tag{8}$$

By transforming the transmission conditions (3) and (5), we get

$$\left(\partial_x + \lambda(s)\right) \widehat{v}^{(k+1)}(b, s) = \left(\partial_x + \lambda(s)\right) \widehat{w}^{(k)}(b, s), \tag{9}$$

$$\left(\partial_x - \lambda(s)\right) \widehat{w}^{(k+1)}(a, s) = \left(\partial_x - \lambda(s)\right) \widehat{v}^{(k)}(a, s), \tag{10}$$

where $\lambda(s) = ps + q$. Inserting (7) and (8) into (9) and (10), we obtain

$$A_v^{(k+1)}(s)D_v(s) = A_w^{(k)}(s)N_w(s), \tag{11}$$

$$A_w^{(k+1)}(s)D_w(s) = A_v^{(k)}(s)N_v(s), \tag{12}$$

where

$$\begin{aligned}
D_v(s) &= \mathrm{i}\kappa(s)\left(e^{\mathrm{i}\kappa(s)b} + e^{-\mathrm{i}\kappa(s)b}\right) + \lambda(s)\left(e^{\mathrm{i}\kappa(s)b} - e^{-\mathrm{i}\kappa(s)b}\right),\\
N_w(s) &= \mathrm{i}\kappa(s)\left(e^{\mathrm{i}\kappa(s)b} + e^{2\mathrm{i}\kappa(s)L}e^{-\mathrm{i}\kappa(s)b}\right) + \lambda(s)\left(e^{\mathrm{i}\kappa(s)b} - e^{2\mathrm{i}\kappa(s)L}e^{-\mathrm{i}\kappa(s)b}\right),\\
D_w(s) &= \mathrm{i}\kappa(s)\left(e^{\mathrm{i}\kappa(s)a} + e^{2\mathrm{i}\kappa(s)L}e^{-\mathrm{i}\kappa(s)a}\right) - \lambda(s)\left(e^{\mathrm{i}\kappa(s)a} - e^{2\mathrm{i}\kappa(s)L}e^{-\mathrm{i}\kappa(s)a}\right),\\
N_v(s) &= \mathrm{i}\kappa(s)\left(e^{\mathrm{i}\kappa(s)a} + e^{-\mathrm{i}\kappa(s)a}\right) - \lambda(s)\left(e^{\mathrm{i}\kappa(s)a} - e^{-\mathrm{i}\kappa(s)a}\right).
\end{aligned}$$

Combining (11) and (12) yields the two-step recurrence

$$A_v^{(k+1)}(s) = G^2(s;p,q)A_v^{(k-1)}(s), \quad \text{where } G^2(s;p,q) = \frac{N_w(s)\,N_v(s)}{D_v(s)\,D_w(s)}.$$

The convergence factor is therefore given after simplification by

$$\rho(s;p,q) = |G(s;p,q)| = \left|\frac{\kappa(s)\,\cos(\kappa(s)\,a) - (ps+q)\,\sin(\kappa(s)\,a)}{\kappa(s)\,\cos(\kappa(s)\,b) + (ps+q)\,\sin(\kappa(s)\,b)}\right|.$$

Next, we consider two optimization strategies for the parameters (p,q), namely, spectral L_∞ and L_2 optimization. The optimization is performed on the imaginary axis $s = \mathrm{i}\omega$, since the relevant modes of the wave equation are oscillatory. The goal is to find parameters minimizing the values of ρ across the relevant frequency band $[\omega_{\min}, \omega_{\max}]$. Since the total simulation time is T, the smallest resolvable nonzero frequency is $\omega_{\min} = \pi/T$; see [4, Figure 3.17]. Due to the discrete time step Δt, the largest frequency that can be represented without aliasing is the Nyquist frequency $\omega_{\max} = \pi/\Delta t$. For the L_∞ optimization, we minimize the global convergence factor $\hat{\rho}_\infty$, i.e.,

$$\min_{(p,q)\in\mathbb{R}^2} \hat{\rho}_\infty, \quad \text{where} \quad \hat{\rho}_\infty = \max_{\omega\in[\omega_{\min},\omega_{\max}]} \rho(\mathrm{i}\omega;p,q),$$

while for the L_2 optimization, we minimize the global convergence factor $\hat{\rho}_2$, i.e.,

$$\min_{(p,q)\in\mathbb{R}^2} \hat{\rho}_2, \quad \text{where} \quad \hat{\rho}_2 = \sqrt{\frac{1}{\omega_{\max}-\omega_{\min}}\int_{\omega_{\min}}^{\omega_{\max}} \rho(\mathrm{i}\omega;p,q)^2 d\omega}.$$

Note that $\hat{\rho}_2$ represents a normalized L_2 norm, in particular the root-mean-square (RMS) value; this normalization ensures that $\hat{\rho}_2$ remains on the same scale as $\hat{\rho}_\infty$, without altering the location of the minimizer. To perform the optimization numerically, we discretize the frequency interval $[\omega_{\min}, \omega_{\max}]$ using a grid of 1000 nodes. For the L_2 criterion, the integral is approximated using the trapezoidal rule (implemented as `trapz` in MATLAB). The minimization is carried out using the

Nelder-Mead simplex method (`fminsearch`), with termination tolerances set to 10^{-4} for both the parameter values (`TolX`) and the objective function (`TolFun`).

3 Numerical Experiments

To validate the parameters obtained by the optimization frameworks discussed in Section 2, we compare them to those minimizing the SWR error after $k = 10$ iterations. To do so, we discretize (1) by the Finite Difference Time-Domain (FDTD) scheme

$$\frac{u_i^{n+1} - 2u_i^n + u_i^{n-1}}{\Delta t^2} + \frac{\gamma}{2\Delta t}\left(u_i^{n+1} - u_i^{n-1}\right) = \frac{c^2}{\Delta x^2}\left(u_{i+1}^n - 2u_i^n + u_{i-1}^n\right)$$
$$+ \frac{\nu}{2\Delta t\, \Delta x^2}\Big[(u_{i+1}^{n+1} - 2u_i^{n+1} + u_{i-1}^{n+1}) - (u_{i+1}^{n-1} - 2u_i^{n-1} + u_{i-1}^{n-1})\Big] + f_i^n.$$

Notice that, for $\nu = 0$, the scheme becomes explicit. To discretize the transmission conditions, we use second-order stencils for both spatial (at $x = b$ and $x = a$) and time derivatives. We choose the following parameters: wave speed $c = 1$, subdomain interface position $a = 0.3$, overlap length $\delta = 0.1$, spatial discretization $\Delta x = 0.002$, temporal discretization $\Delta t = 0.002$, and final time $T = 5$. For these parameters, the discretization error is less than 0.1%. The error between the computed solution $\mathbf{u}_{\text{SWR}}$ and the reference solution $\mathbf{u}_{\text{ref}}$ (FDTD discrete solution) is computed using the relative infinity norm at $t = T$: $\|\mathbf{u}_{\text{SWR}} - \mathbf{u}_{\text{ref}}\|_\infty / \|\mathbf{u}_{\text{ref}}\|_\infty$.

Figure 1 shows the optimized parameters obtained from the L_∞ (green triangle) and L_2 (magenta circle) optimization on the map showing SWR error after 10 iterations. All optimizations are initialized at $(1/c, 0)$ (black square), while the optimal point from the SWR error map is shown as a white square. When $\gamma = 0$ and $\nu > 0$, the computed optimal solutions cluster tightly, and the SWR error map exhibits a pronounced, steep valley around the global minimizer. In contrast, when $\gamma > 0$ and $\nu = 0$, the behavior changes markedly: the error surfaces become much flatter, and the computed minimizers may lie far apart from one another.

We next plot the error curves in Figure 2. We begin with the case $\nu = 0$ and vary the telegrapher damping γ. This corresponds to the first columns of Figure 2. For $\gamma = 4$ and $\gamma = 8$, Figures 2a show that the SWR error exhibits an initial phase where the error increases; this is followed by a rapid drop to machine precision after about 50 iterations. This behavior is typical of SWR applied to the undamped wave equation, for which it has been proved that the number of iterations required for convergence is at least cT/δ [2, 5]. Although this result has been rigorously established for the undamped case with Dirichlet transmission conditions, the observed behavior here suggests that the telegrapher damping shares a similar convergence mechanism. In fact, the chosen transmission conditions, similarly to Dirichlet ones, do not effectively absorb the incoming errors. If one increases γ, the stronger damping mitigates this behavior. In fact, the error curves for $\gamma = 10$ and $\gamma = 12$, using the parameters suggested by the L_∞ strategy, decrease at the beginning for about 10 iterations,

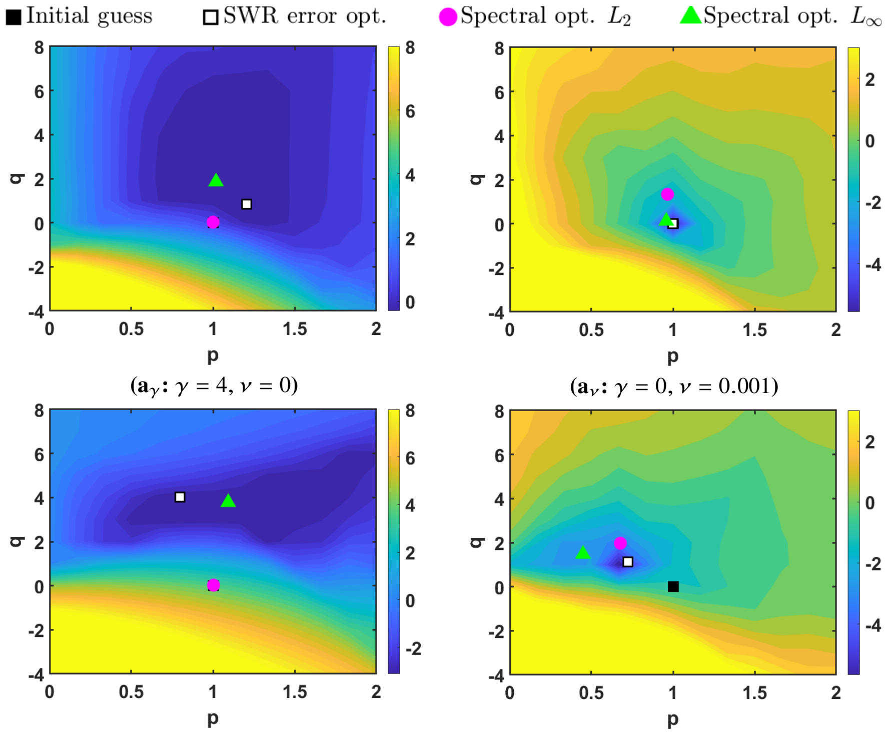

($\mathbf{a}_\gamma$: $\gamma = 4, \nu = 0$) ($\mathbf{a}_\nu$: $\gamma = 0, \nu = 0.001$)

($\mathbf{b}_\gamma$: $\gamma = 10, \nu = 0$) ($\mathbf{b}_\nu$: $\gamma = 0, \nu = 0.05$)

Fig. 1 Performance surfaces showing the final SWR error (log-scale) after $k = 10$ iterations. Left column: increasing telegrapher damping $\gamma > 0$ with $\nu = 0$ (a_γ: $\gamma = 4$, b_γ: $\gamma = 10$). Right column: increasing viscoelastic damping $\nu > 0$ with $\gamma = 0$ (a_ν: $\nu = 0.001$, b_ν: $\nu = 0.05$).

without the initial growth phase, and then grow a little before, eventually, converging to machine precision after about 50 iterations. The initial decay phase is not present if one considers the parameters suggested by the L_2 strategy, which are close to $(1/c, 0)$, and do not lie in the optimality region (see Figure 1).

We conclude that for all telegrapher damping cases, even though the optimized parameters can be close to those minimizing the experimental SWR error (as shown in Fig. 1), SWR does not show a clear linear convergence and it is characterized by a convergence mechanism similar to the one of the (undamped) wave equation.

We now turn to the viscoelastic case, where ν varies while $\gamma = 0$, shown in the second column of Figure 2. The error curves in Figures 2b show a systematic improvement in convergence with respect to the telegrapher damping case. The decay is approximately linear, in contrast to the telegrapher case. The parameter optimization is effective. In all cases, the error eventually reaches the machine epsilon. For $\nu = 0.001$, the curve for the L_∞ strategy converges faster, while for the three other cases, the L_2 strategy provides parameters that exhibit faster convergence.

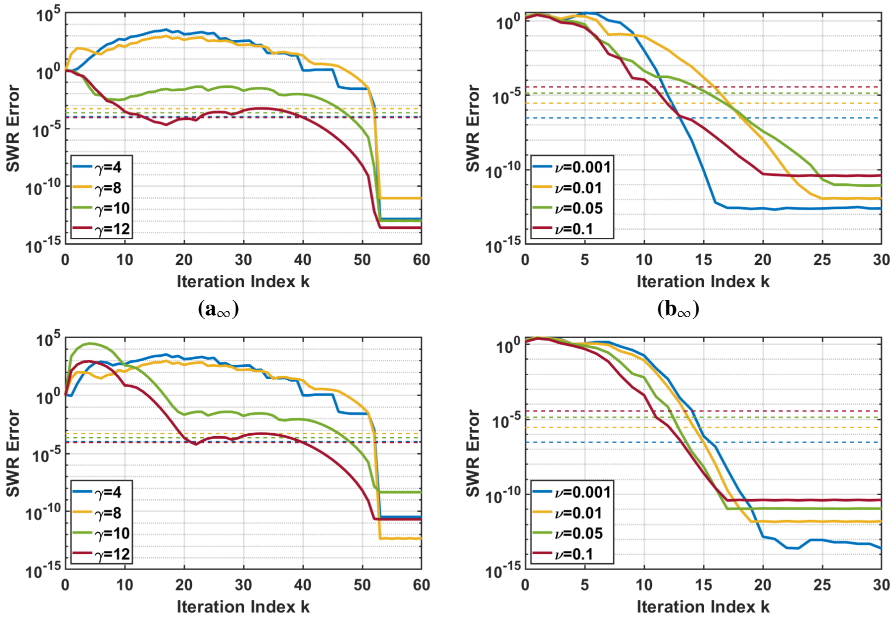

($\mathbf{a}_\infty$) ($\mathbf{b}_\infty$)

($\mathbf{a}_2$) ($\mathbf{b}_2$)

Fig. 2 SWR error curve comparison when varying one damping coefficient at a time. The horizontal axis represents the iteration index k, and the vertical axis represents the relative SWR error on a logarithmic scale. First row: L_∞ strategy. Second row: L_2 strategy. (a) Different values of γ with $\nu = 0$. (b) Different values of ν with $\gamma = 0$. The dashed horizontal line indicates the discrepancy between the full-domain FDTD solution and the analytic ground truth.

In Figures 3 and 4, we illustrate the dependence of the optimal transmission parameters (p, q) on the damping coefficients γ and ν. Figure 3 shows the predicted convergence behavior. Panel (a) shows the global convergence factor $\hat{\rho}$ in the (p, q)–plane, while panel (b) presents a contour map of $\hat{\rho}$ as a function of (γ, ν), with logarithmic axes. The value of $\hat{\rho}_\infty$ decreases when both damping coefficients increase, and variations of ν produce more pronounced reductions. Instead, $\hat{\rho}_2$ increases as ν increases.

The first row of Figure 4 (panels (c_∞) and (c_2)) shows how the optimal pairs (p, q) evolve when γ varies for several fixed values of ν. The second row (panels (d_∞) and (d_2)) displays isolines obtained by varying ν at fixed γ, while the third row (panels (e_∞) and (e_2)) shows isolines produced by varying γ at fixed ν. Both optimization strategies agree that the optimal value of q grows as γ increases. Under the L_∞ criterion, q rises up to approximately 4 for every tested value of ν, whereas in the L_2 case the growth pattern depends on ν, leading to different maximum values of q observed for different damping levels. For both norms, increasing ν causes the optimal value of p to decrease and converge toward a small value, approximately $p \approx 0.05$.

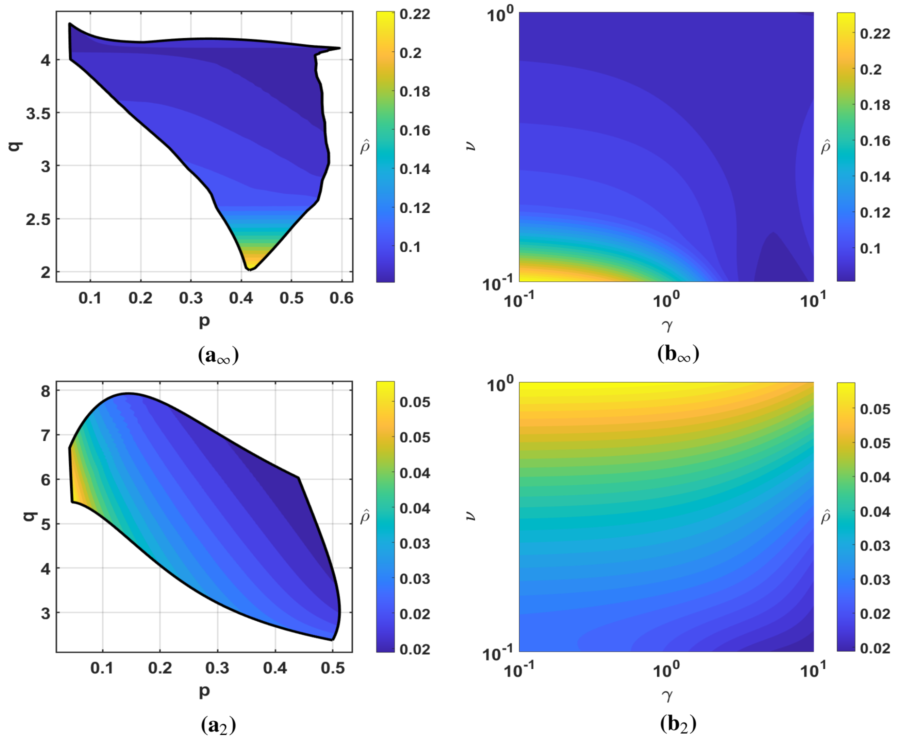

Fig. 3 Predicted global convergence factors $\hat{\rho}_\infty$ (top row) and $\hat{\rho}_2$ (bottom row). (a) Contours of $\hat{\rho}$ in the (p, q)-plane. (b) Contours of $\hat{\rho}$ in the (γ, ν)-plane (log–log axes).

4 Conclusions

We presented an optimization framework for SWR transmission conditions applied to the damped wave equation. We showed that the effectiveness of optimized transmission conditions is strictly dependent on the damping model. For the telegrapher equation, the physics of finite wave propagation speed limits the potential for acceleration, resulting in sublinear convergence regardless of parameter tuning. However, for the viscoelastic damped wave equation, the proposed optimization strategies successfully identify transmission parameters that drastically improve performance. The proposed approach offers a computationally efficient alternative to exhaustive search, ensuring robust convergence rates for viscoelastic problems. Finally, the SWR optimization framework presented here provides a robust basis for accelerating wave simulations in room acoustics and virtual auditory spaces, where real-time performance and computational efficiency are of paramount importance.

Acknowledgements The work of G. Ciaramella and I. Mazzieri has been partially supported by the PRIN2022 grant ASTICE - CUP: D53D23005710006. G. Cicalese, G. Ciaramella, and I. Mazzieri are members of INdAM-GNCS group.

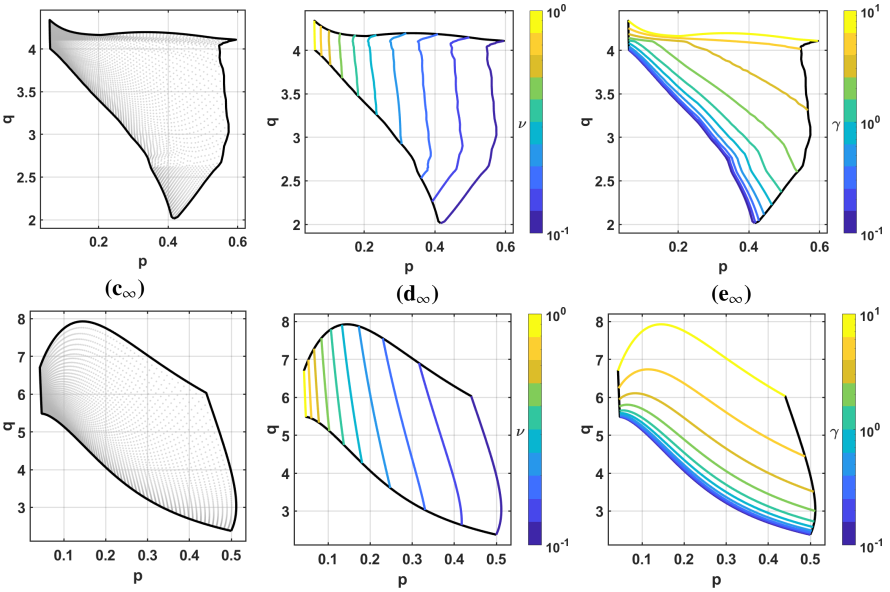

(c∞) (d∞) (e∞)

(c2) (d2) (e2)

Fig. 4 Comparison between the L_∞-optimized (top row) and L_2-optimized (bottom row) transmission parameters. (a) Optimal (p,q) points obtained by varying γ or ν. (b) Isolines of optimal (p,q) for sweeps at fixed ν. (c) Isolines of optimal (p,q) for sweeps at fixed γ.

References

[1] Engquist, B., Majda, A.: Absorbing boundary conditions for the numerical simulation of waves. Math. Comput **31**(139), 629–651 (1977)

[2] Gander, M.J., Halpern, L.: Absorbing boundary conditions for the wave equation and parallel computing. Math. Comput **74**(249), 153–177 (2004)

[3] Gander, M.J., Halpern, L., Nataf, F.: Optimal Convergence for Overlapping and Non-Overlapping Schwarz Waveform Relaxation. In: ”Domain Decomposition Methods in Science and Engineering XI”, vol. 11, pp. 27–36. Springer (1999)

[4] Gander, M.J., Lunet, T.: Time Parallel Time Integration. Society for Industrial and Applied Mathematics, Philadelphia, PA (2024)

[5] Halpern, L.: Schwarz waveform relaxation algorithms. In: Domain Decomposition Methods in Science and Engineering XVII, pp. 57–68. Springer (2008)

[6] Liu, K., Chen, S., Liu, Z.: Spectrum and stability for elastic systems with global or local Kelvin–Voigt damping. SIAM J. Appl. Math. **59**(2), 651–668 (1998)

[7] Zauderer, E.: Partial Differential Equations of Applied Mathematics, 1 edn. Wiley (2006)

MOX Technical Reports, last issues

Dipartimento di Matematica
Politecnico di Milano, Via Bonardi 9 - 20133 Milano (Italy)

10/2026 Dimola, N.; Franco, N. R.; Zunino, P.
Numerical Solution of Mixed-Dimensional PDEs Using a Neural Preconditioner

09/2026 Manzoni, V.; Ieva, F.;Larranaga, A.C.; Vetrano, D.L.; Gregorio, C.
Hidden multistate models to study multimorbidity trajectories

08/2026 Micheletti, S.
Newmark time marching as a preconditioned iteration for large SPD linear systems

Micheletti, S.
Newmark time marching as a preconditioned iteration for large SPD linear systems

07/2026 Corti, M.; Ahern, A.; Goriely, A.; Kuhl, E.; Antonietti, P.F.
A whole-brain model of amyloid beta accumulation and cerebral hypoperfusion in Alzheimer's disease

06/2026 Corti, M.; Gómez, S.
On the compact discontinuous Galerkin method for polytopal meshes

05/2026 Ranno, A.; Ballarin, F.; Lespagnol, F.; Zunino, P.; Perotto, S.
A fictitious domain formulation based on hierarchical model reduction applied to drug-eluting stents

04/2026 Ragni, A.; Cavinato, L.; Ieva, F.
Penalized Likelihood Optimization for Adaptive Neighborhood Clustering in Time-to-Event Data with Group-Level Heterogeneity

03/2026 Mapelli, A.; Carini, L.; Ieva, F.; Sommariva, S.
A neighbour selection approach for identifying differential networks in conditional functional graphical models

02/2026 Antonietti, P.F.; Beirao da Veiga, L.; Botti, M.; Harnist, A.; Vacca, G.; Verani, M.
Virtual Element methods for non-Newtonian shear-thickening fluid flow problems